Journal of Nuclear Materials 538 (2020) 152150

Contents lists available at ScienceDirect

Journal of Nuclear Materials

journal homepage: www.elsevier.com/locate/jnucmat

Revealing the synergistic effects of sequential and simultaneous dual beam irradiations in tungsten via *in-situ* TEM

O. El-Atwani [a, *], W.S. Cunningham [b], J.R. Trelewicz [b, c], M. Li [d], B.D. Wirth [e, f], S.A. Maloy [a]

[a] *Materials Science and Technology Division, Los Alamos National Laboratory, Los Alamos, NM, USA*
[b] *Department of Materials Science and Chemical Engineering, Stony Brook University, Stony Brook, NY, USA*
[c] *Institute for Advanced Computational Science, Stony Brook University, Stony Brook, NY, USA*
[d] *Division of Nuclear Engineering, Argonne National Laboratory, Argonne, IL, USA*
[e] *Department of Nuclear Engineering, University of Tennessee Knoxville, TN, USA*
[f] *Fusion Energy Division, Oak Ridge National Laboratory, Oak Ridge, TN, USA*

HIGHLIGHTS

- Sequential and simultaneous dual beam irradiations have been performed *in-situ* on fine grained tungsten at high temperature.
- Loop damage is quantified as a function of dose or fluence and cavity damage is quantified at the end dose.
- Synergistic effects between sequential and simultaneous beams are revealed.
- Damage evolution is different in all cases.

GRAPHICAL ABSTRACT

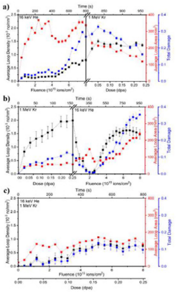

ARTICLE INFO

Article history:
Received 15 January 2020
Received in revised form
2 April 2020
Accepted 3 April 2020
Available online 10 April 2020

Keywords:
Dual beam
in-situ
Dislocation loops
Irradiation damage
Fusion

ABSTRACT

Elucidating the synergistic effects of different energetic beams on the radiation response of nuclear materials is critical for developing an improved methodology for their evaluation when exposed to extreme environments. This article describes *in-situ* sequential (He implantation followed by Kr irradiation and vice-versa) and simultaneous (heavy ion Kr irradiation and He implantation) dual beam irradiations performed on tungsten at 1223 K. Dislocation loop density, average area, and total loop damage as a function of irradiation history and dose/fluence are quantified. The loop Burgers vectors and cavity damage (cavity density, size and total change in volume) are also determined at the final maximum dose for each condition. The loop damage evolution was different in all cases, with the smallest loop damage observed in the simultaneous experiment. Annihilation of Kr generated dislocation loops during He implantation in the Kr + He experiment was an unanticipated observation that may be explained by the dynamic evolution of dislocation loop sink strengths and time-dependent defect fluxes. Dislocation loop raft formation, denuded zones near extended defects, and cavity damage are compared across the different conditions. The phenomena observed and discussed in this work will stimulate further experimental and computational modeling activities leading to improved fundamental understanding of the irradiation response of nuclear materials under reactor-similar environments.

Published by Elsevier B.V.

---

* Corresponding author.
E-mail addresses: oelatwan25@gmail.com, osman@lanl.gov (O. El-Atwani).

https://doi.org/10.1016/j.jnucmat.2020.152150
0022-3115/Published by Elsevier B.V.

1. Introduction

Plasma facing structural components and divertor materials in future fusion devices have to tolerate extreme environments, represented by fast neutrons (~14 MeV which can generate 30–40 dpa/year depending on the neutron wall loading), high particle fluxes involving deuterium and tritium with approximately 10% helium (He) (10^{23}–$10^{24}\,m^{-2}\,s^{-1}$), thermal loads (5–20 MW/m^2), and transient thermal fluxes (e.g., edge localized modes) of several GW/m^2 [1]. Furthermore, 14 MeV neutrons will lead to solid transmutation products (rhenium and osmium in tungsten) and substantial He gas formation in structural materials [2]. For example, He concentrations due to transmutation effects in iron-based structural components could reach levels of about 2000 appm for the anticipated 3–5 year lifetime of a fusion structural component [1] while the high flux of low energy helium ions at the surface of a tungsten-based PFC accelerates surface degradation due to the formation of bubbles, blisters, and nanofuzz [3–7]. These conditions create challenges not only for the testing and evaluation of materials, but more significantly related to the creation of materials that are capable of withstanding these environments [1,8]. Tungsten (W) has widely been considered as a promising divertor candidate due to its favorable characteristics such as a high melting point, good thermal conductivity, low sputtering yield, and low tritium retention [9]. However, severe microstructural changes involving dislocations, dislocation loops, rafts, voids, bubbles, fuzz, etc. [10–14] under different irradiation environments (He plasma, low energy He, or heavy ions to simulate displacement damage) alter W's physical and mechanical properties [8,9], which can ultimately disrupt the operation of a fusion device.

Therefore, designing self-healing radiation tolerant materials and investigating their performance are crucial steps to advancing plasma facing materials (PFMs) for fusion energy. In this context, several innovative routes have been pursued [1]. Formation of nanocrystalline materials [12,15–20] and high entropy alloys [21,22], etc. have been demonstrated with studies on their radiation tolerance under a range of ion irradiation and plasma exposure conditions. However, the majority of irradiation studies on fusion materials use heavy ions to simulate displacement damage from neutron irradiation performed with single beam irradiations, thereby neglecting the synergistic effects of the different particles (He and heavy ions) that PFMs will be exposed to simultaneously in a fusion environment. Simultaneous dual beam irradiations on Fe–9Cr and Eurofer 97 steels have been shown to produce different post-irradiation hardening than sequential He-heavy ion or single beam irradiations [23]. The effects of sequential tungsten and He implantation on nanoindentation hardness of tungsten has also been studied and revealed higher hardness values in the He only implanted regions relative to the sequentially (tungsten then He) implanted material [24]. A fundamental understanding of the response of fusion materials (loop formation and interaction, defect population, threshold for bubble formation) under reactor-relevant conditions employing dual and tri-beam irradiations (where He plasma is considered) is thus a requirement for designing radiation resistant materials and mimic the complex physics of neutron damage. In addition, a fundamental understanding of the damage mechanisms and evolution (loop formation and interaction, defect population, threshold for bubble formation) as a function of irradiation conditions (dose, temperature, etc.) will assist in designing new materials that can withstand fusion conditions.

For this purpose, *in-situ* sequential and simultaneous dual beam irradiation/transmission electron microscopy (TEM) investigations where damage evolution can be observed *in-situ* and quantified post-mortem across many irradiation dose data points can be a valuable tool. Several grades of W have been investigated under different irradiation conditions using *in-situ* TEM/irradiation under single beam irradiation [12,19,25–31]. In these prior studies, loop (interstitial and vacancy type), void (heavy ion irradiations), and bubble (He implantations) formation and evolution have been reported as a function of temperature and dose. Irradiation damage in different tungsten grades (eg. nanocrystalline tungsten and tungsten alloys) has been compared relative to commercial coarse-grained tungsten. However, a comparison of sequential irradiations (He implantation after heavy ion irradiation and vice versa) and simultaneous irradiations (heavy ion and He) to single beam irradiations has yet to be examined.

Here, we describe the results obtained from coarse (average grain size of few micrometers) grained W under simultaneous and sequential beam irradiations via *in-situ* TEM/irradiation at high temperatures (1223 K) where high energy Krypton (Kr) was used to produce displacement cascades and low energy He was used to implant helium and produce isolated Frenkel pair damage. The irradiations were performed for short times to quantify synergistic radiation effects using conditions that produce displacement damage interactions with implanted helium in tungsten as a model BCC material. Defect (loop) size, density, and total damage (product of loop density and average area) evolution was characterized as a function of irradiation dose. Cavity formation and total change in volume after irradiation, as well as the denuded zone formation, were investigated to fully describe the synergistic effects of radiation damage from different energetic particles. The results are of interest to the nuclear materials and nuclear fusion communities working to understand fusion material performance under extreme conditions.

2. Experimental

2.1. In-situ Irradiation/TEM

Thin foils were prepared from bulk tungsten (ESPI Metals, US) via electropolishing using a 0.5% NaOH/water solution at RT. The sample thickness where irradiations were performed and data quantified was ~100 nm (quantified regions were checked with electron energy loss spectroscopy). Samples were irradiated at 1223 K *in-situ* in the intermediate voltage electron microscope (IVEM) with a 300 keV electron beam attached to a Tandem accelerator at Argonne National Laboratory. The temperature was selected to be within the recovery stages for tungsten aided by vacancy migration, which facilitates dislocation loop coarsening (stage III) and annihilation (stage IV) as well as the coarsening of vacancy clusters (stage V) [32]. At the same time, the selected temperature of 950 °C is below the known temperature range for recrystallization of tungsten. The heavy ion was selected to be Kr. Several reasons are behind the choice of Kr ions over self-ion irradiation: 1) The stability of the 1 MeV Kr beam in the IVEM facility ensures a highly reproducible set of irradiation conditions that produce energetic displacement cascades, which is very critical for these types of experiments. 2) To limit the sample heating due to higher energy deposition density during W self-ion irradiation since relatively high temperature measurements were already being performed). 3) To have less implanted ions in the foil since W ion irradiation on W will have a larger fraction implanted and therefore, larger synergistic effects. Therefore, a 1 MeV Kr^{+2} beam was used for the heavy ion irradiation. For the He implantations, a 16 keV He^{+} beam was used. Krypton irradiations were performed to 0.25 dpa and He implantations were performed to have a final implantation of ~1.26% or 12,600 appm (800 s irradiation). For the sequential beam irradiation, the dose rates were ~0.0016 $dpa \cdot s^{-1}$ ($4 \times 10^{11}\,cm^{-2}\,s^{-1}$) for the Kr beam and $1 \times 10^{13}\,cm^{-2}\,s^{-1}$ flux for the He beam. No significant fluctuations in the ion beams fluxes occurred during the experiments.

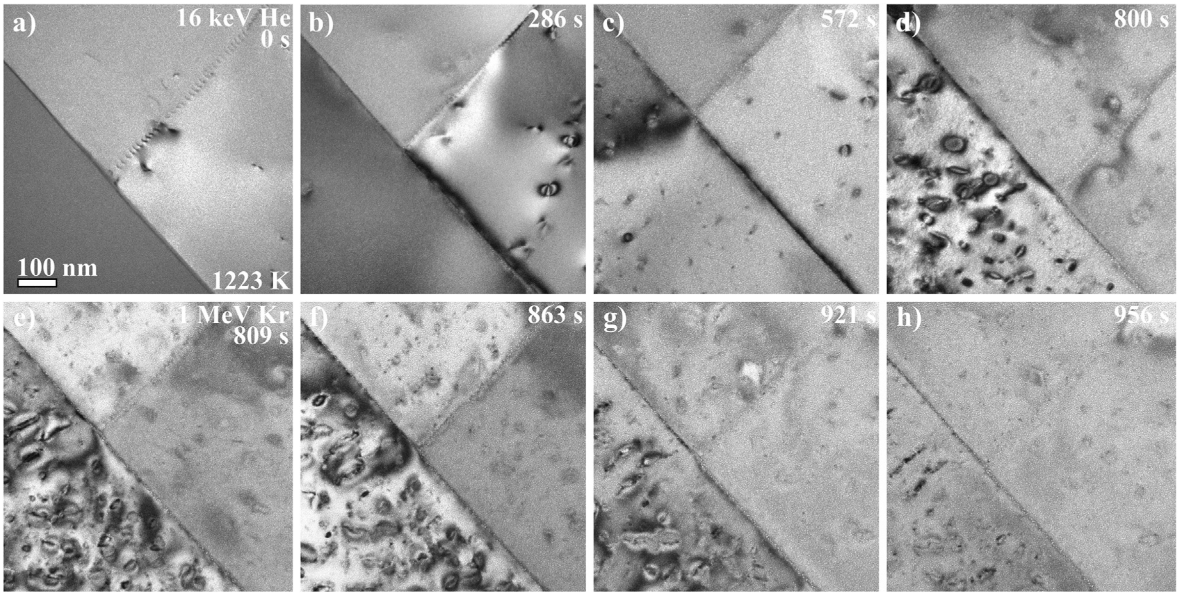

Fig. 1. Bright-field TEM micrographs as a function of time for the sequential (He + Kr) irradiation experiment on W at 1223 K. (a)–(d) *In-situ* 16 keV He^+ implantation. (e)–(h) *In-situ* 1 MeV Kr^{+2} irradiation (following He implantation). Arrows in (e) indicate regions of favorable contrast where loop measurements were acquired. All micrographs have the same scale bar.

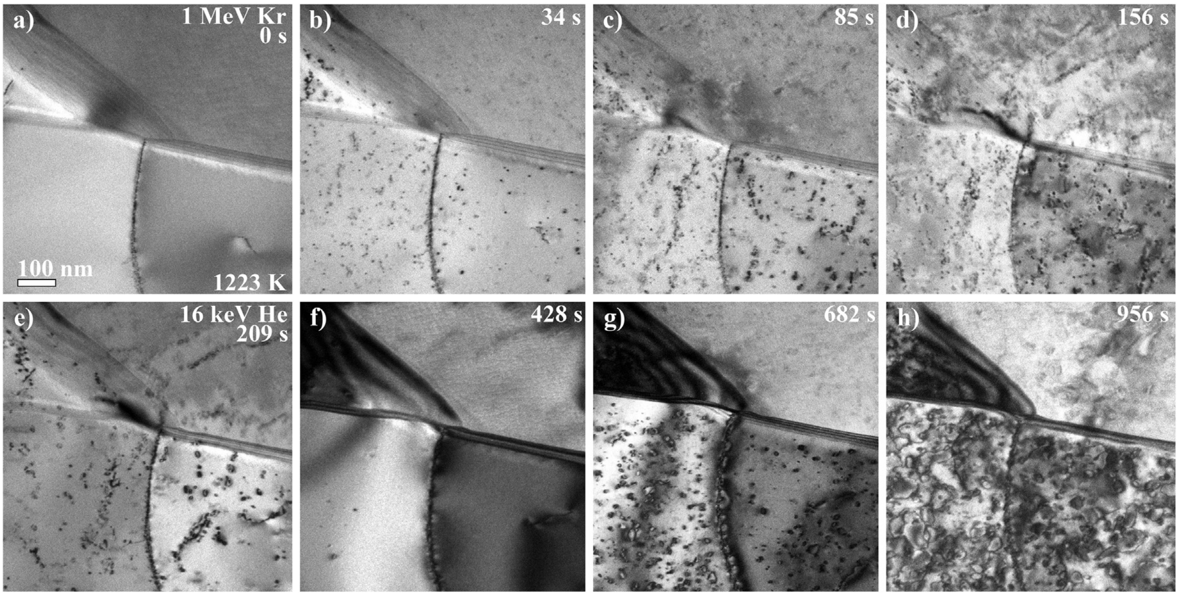

Fig. 2. Bright-field TEM micrographs as a function of time for the sequential (Kr + He) irradiation experiment on W at 1223 K. (a)–(d) *In-situ* 1 MeV Kr^{+2} irradiation (e)–(h) *In-situ* 16 keV He^+ implantation (following Kr irradiation). Arrows in (h) indicate regions of favorable contrast where loop measurements were acquired. All micrographs have the same scale bar.

To achieve the same final irradiation (Kr and He) dose in the simultaneous beam irradiation, the dose rate for the Kr was adjusted to 0.000313 dpa$\cdot s^{-1}$ while maintaining the same He flux. The total irradiation time, in this case, was 800 s. The angle of incidence was 15°. The dpa and ion distributions for both beams are plotted in Figs. S1 and S2 in the supplemental, calculated using the Kinchin-Pease model in the Stopping Range of Ions in Matter (SRIM) Monte Carlo computer code (version 2013) [33] where 40 eV (minimum displacement threshold) [34] was taken as the displacement threshold. While different displacement threshold values (60–90 eV) [34] in W are reported in literature, 40 eV is used in this work to be consistent with other studies used for comparison. The final dose of the Kr irradiation was 0.25 dpa and the final fluence for the He implantation was 8×10^{15} cm^{-2}. It should be noted that in the sequential beam experiments, the second beam was introduced immediately ($\Delta t < 1 s$) following the first beam being switched off to prevent potential defect annealing at the elevated irradiation temperatures.

2.2. Data quantification

To determine the Burgers vector of the loops in the irradiated samples, loops were imaged *ex-situ* under two-beam conditions with <110> and <200> g vectors using an FEI-Tecnai-G2-F30 TEM with

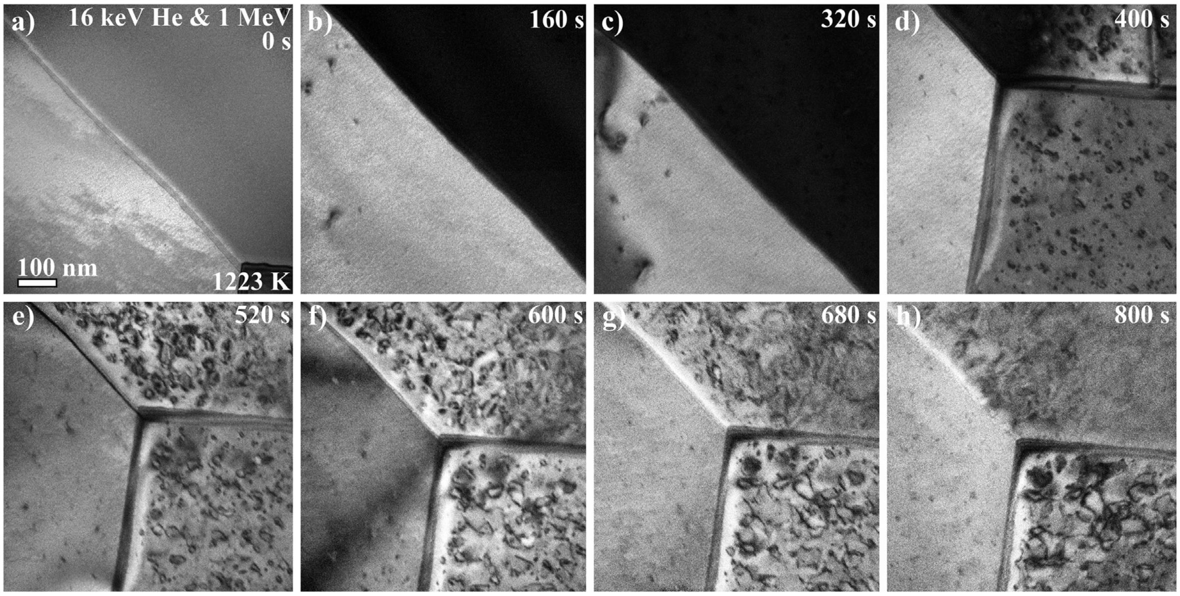

Fig. 3. Bright-field TEM micrographs as a function of time for the simultaneous (He & Kr) irradiation experiment (1 MeV Kr^{+2} irradiation 16 keV He^{+} implantation) on W at 1223 K. The imaged region was moved to a different spot after 320 s due to changes in the diffraction condition. Arrows in (h) indicate regions of good contrast where loop measurements were acquired. All micrographs have the same scale bar.

electron beam energies of 300 keV in the Electron Microscopy Laboratory (EML) at LANL. The Burgers vector percentages, average loop density and area, and average cavity density and area were calculated as detailed in Refs. [35]. Loop areas are reported since not all loops are circular and to calculate the total non-dimensional damage due to loop formation. A measure of total non-dimensional damage was obtained by multiplying the average loop area and density in the 100 nm thick foils. Cavities were characterized using Fresnel under-focused and over-focused imaging and the quantification was performed using the under-focused images (under-focus value was 1.5 μm) where voids appear bright [36] to distinguish the cavities from small loops and avoid over-counting. It should be noted that quantification errors in loop measurements can occur due to image forces, glissile prismatic loop glide to the surface, and changes in foil thickness across the sample [36]. The above factors can affect absolute values but not relative trends, and in this work, focus is placed on comparison of the overall damage trends.

3. Results

3.1. Pre-irradiated sample and experimental conditions

The microstructure of the pristine W sample has been published elsewhere [35] and consists of an equiaxed grain structure with an approximately 2 μm average grain size. The texture is mainly a random type texture with ~50% low angle grain boundaries (LAGB). The main goal of this study is to compare sequential beam irradiations with simultaneous beam irradiations and investigate whether the energetic beam order in the sequential beam irradiations affects defect evolution. Therefore, three experiments were performed:

1) He implantation followed by Kr irradiation (denoted as sequential He + Kr)
2) Kr irradiation followed by He implantation (denoted as sequential Kr + He)
3) Simultaneous He implantation and Kr irradiation (denoted as simultaneous He & Kr)

The choice of 1223 K as the irradiation temperature was made in order to study the most complex situation where all defect types can migrate. While interstitials in W migrate at room temperature (RT) [37], single vacancies and vacancy clusters start migrating at 523 K and 773 K respectively [38]. On the other hand, He-vacancy complexes can migrate at different temperatures depending on their migration energy, which varies based on the ratio of number of He atoms to vacancies [39]. Several complexes, however, need temperatures higher than 1073 K. All experiments were performed near a triple junction with three different adjacent grains. At least one grain was in suitable diffraction conditions for dislocation loop imaging (multibeam imaging where all possible 1/2<111> and <100> loops can be visible since the diffraction conditions involve different g vectors).

3.2. Morphology of the irradiated samples

Fig. 1 shows the bright field TEM images of the sequential He + Kr experiment as a function of time during the *in-situ* TEM/irradiation experiment. Starting with the He implantation to $8 \times 10^{15}\ cm^{-2}$ fluence (Fig. 1a–d), large dislocation loops were formed with different sizes (Video S1 in the supplemental). A loop denuded zone near the grain boundary of the irradiated grain was also noticed. However, no dislocation loop raft formation was observed. The sequential Kr irradiation (Fig. 1e–h) to 0.25 dpa resulted in small loop formation and shrinkage of the existing large loops (Video S2 in the supplemental). The loop denuded zone persisted and raft formation occurred.

Supplementary data related to this article can be found at https://doi.org/10.1016/j.jnucmat.2020.152150.

Fig. 2 shows the bright field TEM images of the sequential Kr + He experiment as a function of time. Contrary to the He implantation of the first experiment, small dislocation loops were formed during Kr irradiation to 0.25 dpa (Fig. 2a–d), which initiated raft formation at ~ 0.025 dpa in agreement with previous raft formation results under heavy ion irradiation on W [13] (Video S3 in the supplemental). No loop denuded zone formation was observed. Upon initiating He implantation (Fig. 2e–h), annihilation

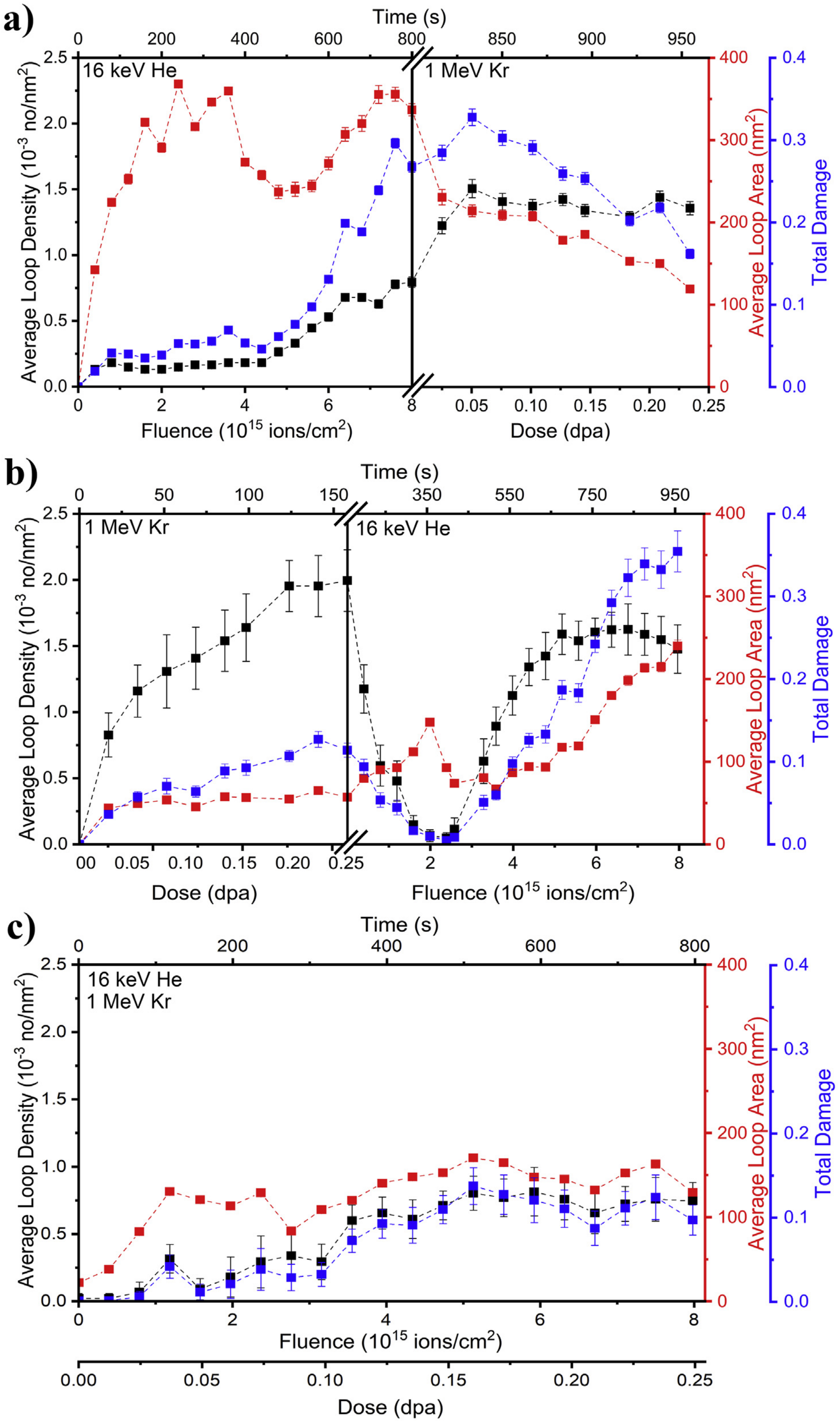

Fig. 4. Comparisons of average areal loop density, loop area and total damage (loop density × loop area) as a function of dpa for the *in-situ* irradiated W at 1223 K for (a) sequential 16 keV He^{+} followed by 1 MeV Kr^{+2}, (b) sequential 1 MeV Kr^{+2} followed by 16 keV He^{+}, and (c) simultaneous 1 MeV Kr^{+2} and 16 keV He^{+}. Error bars are included to reflect errors in quantifying the same area several times.

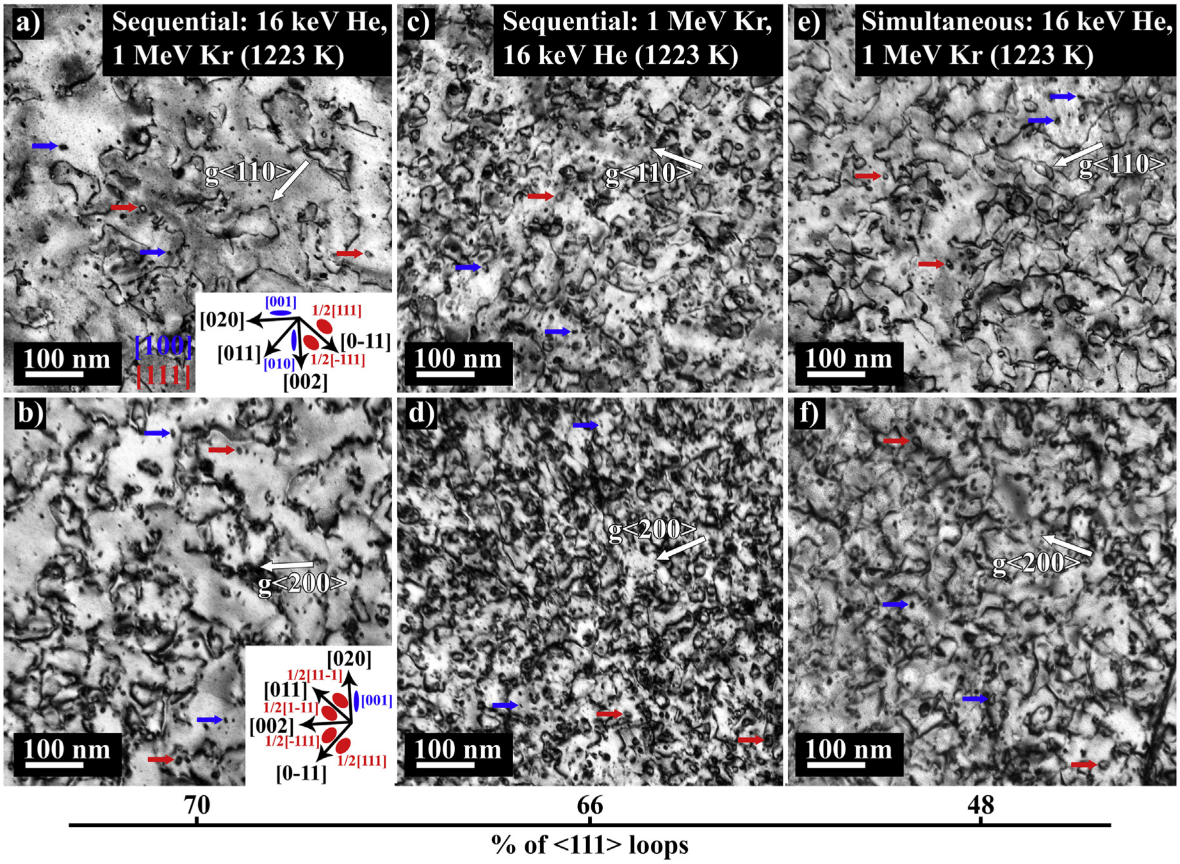

Fig. 5. (a), (c), (e) Bright-field 2-beam TEM micrographs using <110> g vector for the *in-situ* irradiated W at 1223 K for the sequential 16 keV He^+ followed by 1 MeV Kr^{+2}, sequential 1 MeV Kr^{+2} followed by 16 keV He^+, and simultaneous 1 MeV Kr^{+2} and 16 keV He^+, respectively. (b), (d), (f) Bright-field 2-beam TEM micrographs using <200> g vector for the *in-situ* irradiated W at 1223 K at each condition. Images are used to determine the percentages of <111> and <100> Burgers vectors loops (shown at the bottom of the figure) at each condition. Red and blue arrows show examples of ½ <111> and <100> loops respectively, determined using crystallography and ***g.b*** invisibility criteria in the TEM images as described by Yao et al. [43].

of the small loops and rafts and formation of larger loops were observed along with the formation of loop denuded zones (Video S4 in the supplemental).

Supplementary data related to this article can be found at https://doi.org/10.1016/j.jnucmat.2020.152150.

Bright field TEM images of the simultaneous He & Kr irradiations are shown in Fig. 3. Both small and large dislocation loops as well as loop denuded zones were formed (Video S5 in the supplemental). It should be noted that the imaged region in the sample was moved after 320 s due to changes in the diffraction condition (contrast). The bottom grain is then used to quantify the loop damage as it kept its diffraction contrast throughout the irradiation.

Supplementary data related to this article can be found at https://doi.org/10.1016/j.jnucmat.2020.152150.

3.3. Defect and damage evolution due to loop formation

Defect damage evolution is plotted in Fig. 4. Dislocation loop density, average loop size, and total damage due to loop formation (taken as the product of defect density and average size) for the three experiments are shown in the figure.

For the sequential He + Kr experiment (Fig. 4a), dislocation loops began to form immediately after the start of the irradiation. The loop density did not change, however, until after 450 s of implantation (fluence of 4.5×10^{15} cm^{-2}) where a 6 times increase occurred after 3.0×10^{15} cm^{-2} (the density plateaued thereafter). After the start of the Kr irradiation, the density continued to increase (approximately two times at 0.0625 dpa) and reached a plateau where no further change was observed through the end of the Kr irradiation (0.25 dpa). The average loop area, however, increased during He implantation with one observed fluctuation (decrease and then increase again), which can be attributed to a competing effect of new loop formation and growth of existing loops. During the Kr irradiation, a decrease in the average loop area occurred. The total damage followed the trend of the loop density during He implantation and the trend of the average loop area during the Kr irradiation.

For the sequential Kr + He experiment (Fig. 4b), the loop density demonstrated an increase from the beginning of the Kr irradiation and reached a plateau at approximately 0.2 dpa. During subsequent He implantation, the average loop density dropped to zero (i.e., loops were annihilated) at ~2×10^{15} cm^{-2}, followed by an increase and a plateau at a fluence of 5.0×10^{15} cm^{-2}. The loop area, however, did not show any change during Kr irradiation, but increased during He implantation at the point of loop annihilation (only a few large loops remained). The average loop area then decreased to the same value as the Kr irradiation and increased rapidly again. The total damage trend followed the average loop area trend during Kr irradiation and the loop density trend during He implantation up to the saturation point in which the average loop area change governed the total damage.

For the simultaneous irradiation (Fig. 4c), loop density and average size increased with similar trends as a function of time and plateaued after 500 s, which corresponds to a fluence of

$5.0 \times 10^{15}\,\mathrm{cm}^{-2}$ (He implantation) and total dose of 0.156 dpa (Kr irradiation). The total damage followed the same trend as the loop density and average loop size.

The consistency of the results (loop density and average size) across different *in-situ* TEM/irradiation runs can be elucidated by comparing with previous single beam irradiations (1 MeV Kr^{+2}) results on the same tungsten grade at the same dpa (Fig. 2 in Ref. [40]). At 0.25 dpa, loop density and size were in remarkable agreement to the values in this work. This consistency is attributed to the stable beam conditions during the experiments and due to following a consistent defect quantification procedure [35].

3.4. Dislocation loop Burgers vector analysis

Part of the goal of this study is to determine the Burgers vector and percentage of each loop type at the end of each experiment. In W, dislocation loops of either 1/2<111> and <100> type can be present as determined from previous experimental and simulation studies [29,30,35,41]. *Ex-situ* imaging using g<200> and g<110> diffraction beams (Fig. 5) was performed for each experiment from which the total loop density is analyzed. Since different dislocation loop variants can be observed under different diffraction conditions, two equations with two unknowns (% of 1/2<111> loops and % of <100> loops) can be solved to determine the Burgers vector percentage in each experiment. This methodology is consistent with that used previously in W by several groups [29,35,42]. The results are presented in Fig. 5. In addition, by using the combination of crystallographic information (including loop projections) and ***g.b*** invisibility criteria as described by Yao et al. [43], we can demonstrate in Fig. 5 that both ½ <111> and <100> dislocation loops coexist in the sequential and the simultaneous experiments.

4. Discussion

4.1. Nature of the dislocation loops

The nature of the dislocation loops formed under sequential and simultaneous irradiations are of importance, as they affect the overall damage evolution noted in the prior section. As shown in Fig. 5, the percentages of <111> dislocation loops in the sequential experiments were similar, but differed from the simultaneous irradiation experiment. In the sequential Kr + He experiment, the dislocation loops from Kr were first annihilated during He implantation. However, loops generated after He implantation only (Fig. S2 in the supplemental) showed a similar <111> percentage to the sequential He + Kr experiment. There is an outstanding question related to the recent results from Harrison et al. [31,44], which showed no <100> loop formation during similar energy He implantation in W at temperatures up to 1023 K. However, the fact that 16 keV He^{+} implantation at 1223 K resulted in <100> loop formation suggests other mechanisms (e.g., not directly from the cascades) must be responsible for the formation of <100> loops. Eyre-Bullough suggested that loops can nucleate to form <110> Burgers vector loops with enclosed stacking faults that shear to form either ½ <111> loops or <100> loops, which is known as the Eyre-Bullough mechanism [45]. However, several *in-situ* studies [19,30], including this one, have not observed faulted loop formation. In addition, un-faulting to <100> loops was shown to be highly unlikely [46]. Moreover, the high stacking fault energy of BCC metals means that stable faulted loop formation is not possible. Interaction and reaction between 1/2<111> loops to form <100> loops was described by Marian and Wirth [47]. Through molecular dynamic simulations, it was shown that 1/2<111> Burgers vector loops of the same size interact with one another in steps to form <100> loops. Another applicable mechanism is the reaction of two ½<111> loop variants to produce a <100> loop [48]. The high mobility observed during the He implantation in this work suggested that such a mechanism is actually plausible (Videos S1 and S4 in the supplemental).

4.2. Comparison of defect and damage evolution

4.2.1. Sequential irradiation experiments, He + Kr

Dislocation loop formation during He implantation in the first experiment (sequential He + Kr) is significantly larger than those formed during Kr irradiation, based on the total damage parameter (the product of loop areal density and loop area). The final displacements per atom (dpa), however, were nearly the same (0.25 dpa for Kr and 0.35 dpa for He as shown in Figs. S1 and S2 in the supplemental). During the 16 keV He implantation, approximately fifteen Frenkel pairs were generated for every implanted He ion, although the predicted number of Frenkel pairs is sensitive to the displacement energy used in the SRIM calculation. Vacancies will form complexes with He and the concentration of these He-vacancy complexes is predicted by computational modeling to rapidly increase in a very short period of time [49,50] after the collision cascade due to the fast migration of He. The He-vacancy complexes are stable and grow at a later stage to He bubbles via the absorption of helium, vacancies, or via trap mutation reactions (emitting interstitials) [51,52]. The latter mainly occurs when the helium clusters, or bubbles, are over pressurized and there is a small supply of vacancies, which is not the case in this study. The growth of these complexes to bubbles via vacancy absorption is expected to decrease interstitial-vacancy recombination and correspondingly, result in a large interstitial concentration in the grain matrix (compared to conditions with no He-vacancy complex formation as in the case of the Kr irradiation in the sequential Kr + He experiment). Thus, once interstitial type dislocation loops have nucleated, the flux of interstitials to these loops will produce larger dislocation loops and lower densities. Moreover, due to the production of a high density of Frenkel pair defects by He ion irradiation, self-interstitial cluster and a/2<111> dislocation loops have high mobility and can interact and coalesce leading to large dislocation loops. During He implantation, bubbles were shown to form on the grain boundary and within the grain matrices before loop formation was observed to occur (Video S1 in the supplemental). About 50 s was needed for visible dislocation loops to begin to form, an expected effect of loop nucleation and growth from Frenkel pairs (which requires an incubation period).

During Kr irradiation in the sequential He + Kr experiment, the average loop area was observed to decrease, while the loop density increases. We believe this is due to two reasons. First, Kr ion irradiation produces new, smaller dislocation loops [35] directly in collision cascades [32], which will decrease the average loop size and increase the loop density. This mechanism is consistent both with this *in-situ* TEM work as well as prior studies in which loops were shown to form just after the start of the irradiation process [26]. The loop size distribution at small sizes was consistent with that measured following the Kr ion irradiation in the sequential Kr + He experiment (Fig. 4 b), and growth of the loop area was not observed like it was in the case of He implantation in the sequential He + Kr experiment. Second, the large dislocation loops formed after He implantation were observed to shrink (Video S2 in the supplemental). The shrinkage of these loops may result from cascade overlap and the resulting dissolution (recombination) by Kr ion-induced heavy (large PKA energy) cascades [53,54]. Indeed, Capps performed molecular dynamics (MD) simulations and observed that collision cascades initiated with PKA energy of 5 or 10 keV can lead to a notable decrease in the size of a 91 interstitial loop with a/2<111> Burgers vector that was trapped by multiple helium interstitials in body centered cubic iron [55]. While that study did not evaluate PKA energies larger than 10 keV, it does indicate that a high-energy displacement cascade overlap with pre-existing dislocation loops can lead to a reduction in loop area, although clearly additional simulation work is required to confirm this behavior in tungsten at PKA energies representative of the 1 MeV Kr ion irradiation.

Shrinkage of loops (self-trapped by long range elastic interaction) in W due to interactions with opposite type loops has also been reported in ion irradiated thin films [56]. MD simulations of displacement cascades in W have shown formation of both interstitial and vacancy type loops directly from cascades [41], and thus, interactions between these small loops and the large loops created by He ion irradiation is possible. However, the remaining loops from the Kr irradiation (after first performing He irradiation) were still larger than those created from Kr irradiation with no pre-implanted He (sequential Kr + He experiment). This observation is not fully consistent with the smaller loop sizes after W irradiation on W with pre-implanted He as reported by Harrison et al. [30]. The discrepancy can be attributed to the He fluence used during pre-implantation. For example, in our work, we observed shrinkage of the loops, but the loops after He implantation were already large (~350 nm^2) prior to heavy ion irradiation. In addition, W irradiation on W produces even heavier cascades than Kr on W, and it is possible that the cascade overlap induced shrinkage could be even larger. The other difference in these two studies is the temperature. Harrison and co-workers performed the helium pre-implantation at RT, for which the diffusivity of vacancies and He-vacancy complexes is much reduced relative to the much higher temperature of 1223K used in our study, therefore affecting the overall size of the dislocation loops formed during implantation.

4.2.2. Sequential irradiation experiments, Kr + He

During the initial Kr irradiation in the sequential Kr + He experiment, the loop density increased with time but maintained a nearly constant loop area that was considerably smaller than during the initial He irradiation in He + Kr sequential irradiation. Upon He implantation in the sequential Kr + He experiment, the loop density dramatically decreased from 2×10^{-3} to $0.05 \times 10^{-3}\,nm^{-2}$ with an increase in loop area from ~60 to ~150 nm^2. These changes presumably result from loop annihilation (recombination) of the relatively small dislocation loops, in which only relatively large loops remain. The annihilation of the dislocation loops at this stage is the most notable phenomenon in the sequential Kr + He experiment. While it is not immediately clear how to explain this behavior, it is possible that competing mechanisms of interstitial and vacancy defect absorption first produce loop annihilation, with subsequent loop re-nucleation, although a more detailed computational modeling study is required in the future.

In considering this possibility, it should first be mentioned that loops observed to form during Kr irradiations have both a/2<111> and a<100> Burgers vectors. Dislocation loops formed under high-energy PKA induced displacement cascades in W have been shown to be of both interstitial and vacancy loop type. For example, MD simulations by Setyawan et al. [41] have shown the formation of vacancy type <100> loops, in addition to self-interstitial loops of both a/2<111> and a<100> Burgers vectors, which form directly in high-energy cascades at both room temperature and the elevated temperature of 1023K. El Atwani et al. [35] have shown that the <100> types loops in heavy ion (Cu^+) irradiated W are relatively small in size (less than 4 nm) and sessile in nature. Yi and co-workers [28,29] have indicated that ~60−90% (varies depending on the irradiation temperature and heavy ion energy) of the a/2<111> loops have interstitial character following either 2 MeV or 150 keV self-ion irradiation at 1023 or 1073 K, respectively. Thus, following the completion of the Kr ion irradiation, we believe that the majority (~2/3) of the dislocation loops have a Burgers vector of a/2<111>, as indicated by Fig. 2 and the loop migration and raft formation shown in the video (supplementary material), and that these <111> type loops are predominately interstitial character (~80% of the a/2<111>). However, we also expect that a non-negligible fraction (~1/3) of the loops have a Burgers vector of a<100>, and that these loops are predominately vacancy character (~90% of the a<100>).

During helium ion irradiation, isolated Frenkel pairs as well as a high density of small helium-vacancy clusters are expected to form. At the irradiation temperature of 1223 K, both the interstitials and vacancies are mobile, although the interstitials have a much higher diffusivity. Assuming that approximately, 1/3 of the existing dislocation loops have a Burgers vector of a<100>, and of these, about 90% have vacancy character while the remainder are of interstitial type, then we can quantify the point defect sink strength of the different loop populations. Table 1 provides an estimate of the sink strength for point defect absorption at the dislocation loops, assuming that the <111> and <100> loops both have the same average size of 4.0 nm diameter, and that the capture radius of a dislocation loop with a Burgers vector of a<100> is larger than that of an a/2<111> loop, with a multiplication factor of 1.5x. The assumption of a 50% larger capture radius for an a<100> loop is based on scaling the capture radius with the Peach-Koehler force that defects would experience in the presence of a prismatic dislocation loop. The Peach-Koehler force scales with shear modulus times the magnitude of the Burgers vector squared (Gb^2) [57]], and also depends on the dislocation core energy. Thus, the difference in magnitude of the square of the Burgers vector between an a<100> and an a/2<111> dislocation loop provides a factor of 1/0.75 (4/3). Additionally, consideration of the BCC geometry of tungsten indicates that both the absolute loop size (effective radius versus number of SIA contained in a given loop) and the dislocation core radius should be larger for an a<100> than an a/2<111> prismatic loop. Consequently, we have assumed, as a first-order estimate, that the a<100> prismatic dislocation loop will have a 50% larger interaction/capture radius for the a<100> prismatic loop.

We should also point out that the interaction radius for absorbing self-interstitials should be larger than that of vacancies, irrespective of loop Burger vector or the vacancy/interstitial character of the loop. The consideration of the sink strength of the dislocation loop populations leads to the conclusion that the sink strength for the vacancy a<100> loops is comparable to, and even larger than, the interstitial a/2<111> loops. Since the interstitials are more mobile than the vacancies, although both are quite mobile at 950 °C in W, and have a larger interaction radii than vacancies, it is natural to expect shrinkage and annihilation of the vacancy a<100> as a result of the initial preferential absorption of the interstitial flux at the vacancy loops. Such annihilation will reduce the sink strength of vacancy a<100> loops, which would then make the a/2<111> interstitial loops the dominant sink for absorption of the mobile vacancies, which would also result in their shrinkage. We can envision that this process of effective annihilation through the preferential absorption of interstitials at vacancy type a<100>, and then vacancies at interstitial type a/2<111>, loops could dynamically cycle until the majority of the interstitial and vacancy loops have been annihilated. This dynamic annihilation process would produce dissolution and shrinkage of the loops to very small densities, with preferential growth of the lower density loops to larger sizes as loop density (and sink strength) decreases. Of course, this proposed sequence of events requires further research and substantiation through detailed mesoscale modeling that includes

Table 1
Calculated dislocation loop sink strengths.

Loop type	Density (m^{-3}), based on assumed 100 nm foil thickness	Loop size (nm)	Relative capture radius (in units of $r_{capture}^{\frac{a}{2}<111>}$)	Sink strength (m^{-2})
interstitial, a/2<111> – assumed 80%	1.1×10^{22}	4.0	1.0	1.4×10^{14}
vacancy, a/2<111> – assumed 20%	2.6×10^{21}	4.0	1.0	0.33×10^{14}
interstitial, a<100> –assumed 10%	6.8×10^{20}	4.0	1.5	0.13×10^{14}
vacancy, a<100> – assumed 90%	7.7×10^{21}	4.0	1.5	1.5×10^{14}

the dynamic evolution of the loop sink strengths (size and density) with the concurrent helium ion irradiation, which we plan in the future.

Thus, we believe that a plausible explanation of the significant decrease in loop density upon initiating the 16 keV helium ion irradiation is that the initial annihilation of vacancy loops results from the preferential flux of interstitials to these a<100> vacancy loops, driven by the higher relative interstitial concentrations resulting from the formation of helium-vacancy complexes, and the larger relative bias/sink strength of the a<100> loops. Fig. 6 (and Video S6 in the supplemental material) shows a series of time snapshots observed in the TEM during the He irradiation that shows loop shrinkage, although future work will be required to verify these hypothesis. The assumption of the larger sink strength of the a<100> loops shown in Table 1 is consistent with recent analysis of dislocation bias factors and sink strengths discussed by Kohnert and Capolungo [58], although further atomistic modeling analysis will be required to confirm the details of the relative capture radius of a<100> versus a/2<111> loops for both vacancies and interstitial type defects.

Supplementary data related to this article can be found at https://doi.org/10.1016/j.jnucmat.2020.152150.

Once the loop density has dropped sufficiently as a result of these recombination/annihilation processes, we believe that renucleation of interstitial type, a/2<111> loops can occur under the helium ion irradiation, and these newly formed loops can grow due to the lower loop density and super-saturation of interstitials relative to vacancies. The incubation period for loops to form during initial He implantation in the sequential He + Kr experiment was ~50 s while ~180 s was needed for loop formation during He implantation in the sequential Kr + He experiment (just after the annealing of Kr irradiation induced loops). This implies that the interstitials created during He implantation in the sequential Kr + He experiment reached a critical concentration for loop formation at later times than the He implantation (without Kr pre-irradiation) and supports the idea that annihilation of these interstitials initially occurred with vacancy loops or vacancy clusters.

4.2.3. *Simultaneous irradiation experiment*

In the simultaneous irradiation experiment, both loop density and size increased from the beginning of the irradiation, and then saturated at ~0.7×10^{-3} nm^{-2} and 150 nm^2 respectively, with an overall damage of ~0.1 after about 400 s that corresponds to a 0.125 dpa Kr and 2×10^{16} cm^{-2} He fluence. In comparison, during the Kr irradiation in the sequential Kr + He experiment, 125 s were needed for the density to reach saturation at a higher density of 2.0×10^{-3} nm^{-2} (~2.8 times the density in the simultaneous He & Kr experiment). However, the average area saturated nearly from the start of the irradiation at ~50 nm^2 (~3 times less the simultaneous experiment) and the overall damage was nearly the same. After He implantation in the sequential Kr + He experiment, the density, size, and overall damage initially decreased substantially, before increasing again but producing higher values of density and loop area than the simultaneous experiment. Additionally, only the loop density saturated while the loop area continued to increase and thus, the overall damage did not saturate. During He implantation in the sequential He + Kr experiment, no saturation was observed in the average loop area or the overall damage while density trended towards a saturation value (~0.7×10^{-3} nm^{-2}) similar to the simultaneous He & Kr experiment. The trends in this part of the experiment appear similar to the trends in the He implantation in the sequential Kr + He experiment but with a significant difference in magnitude. While the density was lower by a factor of ~2, the loop size was higher by a factor ~1.45. This suggests an effect of the pre-existing defects during Kr irradiation in the sequential Kr + He experiment even though the loops were annihilated before He implantation induced loop formation started to occur.

In the MD simulations of cascade overlap performed by Capps, the existence of pre-existing vacancies were shown to impact both the absolute number of newly created Frenkel pairs, as well as the amount of interstitial clustering in such a way that the absolute number of new defects was decreased but with a slightly increasing fraction of interstitial clusters [41]. More research is clearly needed to develop a larger database, as well as to evaluate this effect with

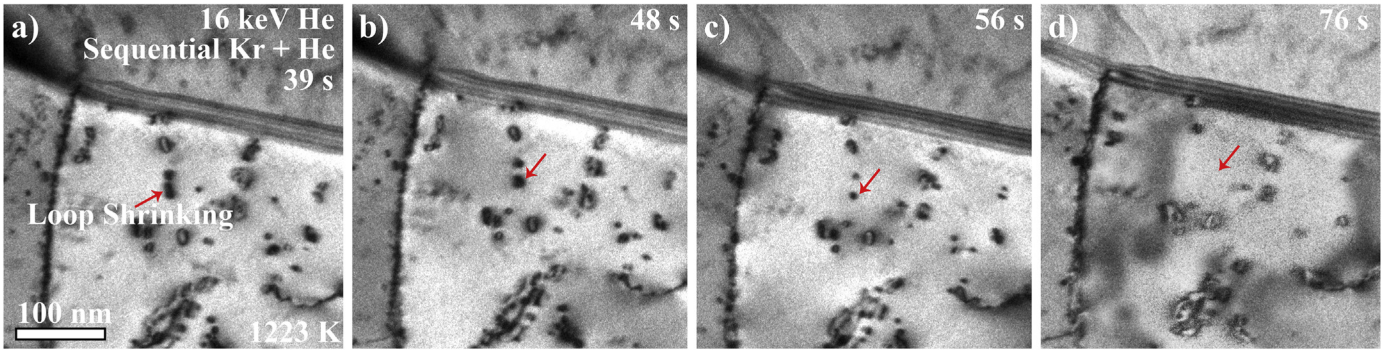

Fig. 6. Bright-field images of loop shrinkage and annihilation during He implantation in the sequential Kr + He experiment.

higher energy PKAs. El Atwani et al. has shown void formation in heavy ion irradiated W at similar temperatures and dpa [35]. It is therefore evident that pre-existing voids and defect density have a noticeable effect on defect evolution during irradiation. The defect morphology evolution after Kr irradiation (in the sequential He + Kr experiment) differed slightly from the simultaneous He & Kr experiment. From the data in this work, it is evident that the overall damage in the simultaneous experiment is smaller than in the sequential experiments, but with different defect evolution trends (Fig. 4). The overall damage (total damage) in the simultaneous experiment is closer to the sequential He + Kr case while the dislocation loop damage evolution trends are similar to the single beam (Kr irradiation in the sequential Kr + He experiment). The sequential experiments, on the other hand, demonstrated different defect evolution and overall damage behavior from each other. The results are compared for three different samples with different grain boundaries. However, the possible differences in the grain boundary character is assumed to be insufficient to affect the trends or the values tremendously. Therefore, the *in-situ* nature of the experiments allowed for the determination of a detailed morphology evolution and demonstrate the importance of having a testing protocol for nuclear materials that mimic real reactor conditions.

4.3. Dislocation loop denuded zones

Loop denuded zone formation is another relevant phenomenon since it represents both the sink efficiency of grain boundaries, which have been shown to depend on irradiation parameters, and the defect diffusion characteristics, in addition to macroscopic degrees of freedom of a grain boundary [59]. Recently, El Atwani et al. has shown that no denuded zone formation occurs in heavy ion irradiated W but it does occur in He implanted W [59]. Such an effect was described to depend on the differences between defect (interstitial and vacancy) mobilities. During heavy ion irradiation, interstitials in W are very quick to saturate a grain boundary, which has been shown to require some vacancy flux for extra recombination at the grain boundary and for denuded zones to form. Vacancies are relatively slow diffusers in W and thus no denuded zones are shown to occur up to 1073 K. During He implantation, He bubbles and He-vacancy complexes were shown to slow down interstitials [60,61], thus allowing extra recombination to occur on grain boundaries and encouraging the formation of loop denuded zones. In this work (Fig. 2), no denuded zones were formed during Kr irradiation in the sequential Kr + He experiment. However, after He implantation, loop denuded zones were observed in the sequential and the simultaneous experiments. In addition, the Kr irradiation after He implantation still resulted in denuded zone formation. The results appear to be in agreement with the prior work by El Atwani et al. that bubbles and He vacancy complexes can slow down interstitials to form loop denuded zones in W.

4.4. Rafting

Rafting was also shown to occur in heavy ion irradiated W [13,28,62]. In this series of experiments, rafting was only observed during single beam Kr irradiation (during Kr irradiation in the sequential Kr + He experiment). This can be explained by the loop size. Small loops are able to rotate their Burgers vector and glide rapidly to be self-trapped in a raft [63]. The small loops formed after Kr cascades fulfill the conditions of raft formation unlike loops formed after or during He implantation where interstitials from Frenkel pairs agglomerate to form large loops. The results can also suggest that Burgers vector rotation could be an outcome of small loop interactions with the heavy ion cascades. The energy deposited from heavy ion cascades can presumably cause rotation of small loops unlike the low energy He ions (which can only cause Frenkel pair generation), although this requires future confirmation that will likely require atomistic modeling as well as further *in-situ* TEM observations.

4.5. Cavity damage (bubble and void)

Irradiation damage is not only represented by dislocation loops. Cavities (bubbles and voids) affect the mechanical properties and are considered moderate barriers which harden the materials more than dislocation loops in W [64]. Fig. 7 shows Fresnel bright field images (underfocused where bubbles appear bright) of coarse-grained W with the sequential and simultaneous beams. Fig. 8 shows the cavity density, average cavity area, and the commonly used correlation between cavity population and estimated volumetric swelling (using $\Delta v/_{v} = \frac{4}{3}\pi\ r_c^3 N_v$ where N_v is the cavity density in a 100 nm thick foils and r_c is the radius of the cavity) in the grain matrices at the final doses for the experiments in this study, as well as for single He implantations at 1223 K (same temperature and final fluence in this study which will be published elsewhere). The figure also shows the void damage from heavy ion irradiation only at 1050 K [35]. The sequential experiments led to approximately similar cavity densities and sizes and thus similar overall changes in volume. The simultaneous beam irradiation experiment,

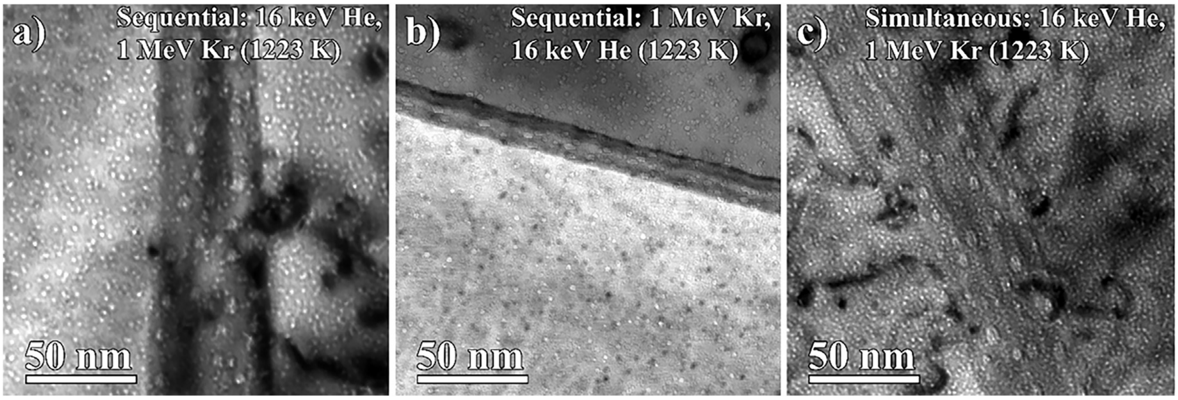

Fig. 7. Bright-field TEM micrographs illustrating cavity dispersions and sizes in the *in-situ* irradiated W under the following conditions: (a) sequential 16 keV He^+ followed by 1 MeV Kr^{+2} at 1223 K, (b) sequential 1 MeV Kr^{+2} followed by 16 keV He^+ at 1223 K, (c) and simultaneous 1 MeV Kr^{+2} and 16 keV He^+.

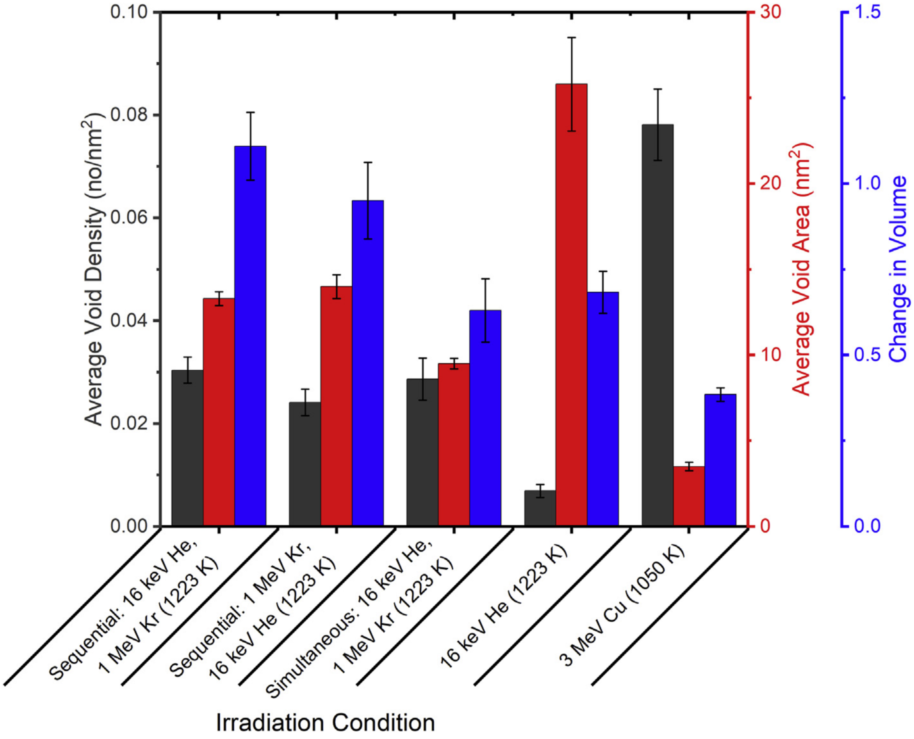

Fig. 8. Comparisons of average areal cavity density, cavity area and total change in volume for different irradiation conditions on W at 1223 K. Values for the 3 MeV Cu$^+$ irradiation at 1050 K are from Ref. [35].

however, resulted in lower average sizes and total change in volume by a small factor (~1.5–1.75 times less). The He only condition resulted in a lower cavity density but larger cavity size (all experiments where Kr was included) and an overall similar change in volume to the simultaneous He & Kr experiment. The inclusion of Kr at any point of the irradiations led to smaller cavity sizes but larger densities. This is expected as it has been shown that Kr or heavy ion irradiation leads to smaller, but higher density, cavities [40]. These cavities are believed to form from the growth of vacancy loops or vacancy clusters formed directly from the cascades as illustrated earlier. A 3 MeV Cu$^+$ irradiation to 0.25 dpa (similar to the experiments in this study) at 1050 K is shown in the figure and demonstrates higher density but smaller cavity sizes and an overall lower change in volume. All grain boundaries (Fig. 7) demonstrated larger cavity sizes, suggesting He trapping by the grain boundaries.

5. Conclusions

Fusion reactor materials will be exposed to simultaneous neutron irradiation and particle implantation. The synergistic effects of different energetic particle beams need to be fundamentally understood and experimentally tested on related materials for improved evaluation of the material irradiation response. In this study, *in-situ* sequential (He implantation followed by Kr irradiation and vice-versa) and simultaneous heavy ion Kr irradiations and He implantations are performed on tungsten at 1223 K. Loop density, average size and total loop damage (product of loop density and size) are quantified as a function of dose/fluence. Loop type and cavity damage at the end dose are also quantified. The conclusions are as follows:

- Both ½ <111> and <100> loops existed in the sequential and simultaneous experiments but with different percentages. Even for pure He implantation, <100> loops were shown to form.
- The loop damage evolution (density, size and total damage) trends are different in every case. The total loop damage is smallest in the simultaneous experiments.
- In the Kr + He sequential experiment, all dislocation loops after Kr irradiation were annihilated during the start of He implantation. Subsequently, after the significant decrease in loop density, the nucleation of new dislocation loops due to He implantation was observed, and these loops grew to large sizes. A plausible explanation explaining the loop annihilation is the time dependent partitioning of interstitials to vacancy-type a<100> loops, followed by vacancy absorption at interstitial type a/2<111> loops. However, future research will be required to confirm this hypothesis.
- Rafting was observed only when heavy ion irradiation was involved. This is justified by the presence of small loops during Kr irradiation (which can rotate their Burgers vector to form rafts) and possibly due to the high-energy deposition during Kr cascades, which can promote Burgers vector rotation.
- Denuded zone formation was observed only after or during He implantation. This is believed to involve a mechanism in which He and He bubbles slow down interstitial migration, which in turn promotes enhanced recombination of interstitials and vacancies on the grain boundaries.
- While the cavity damage trend was the same in all experiments, the smallest change in volume was shown to occur in the simultaneous experiment and the sequential Kr + He. The simultaneous experiment had a different cavity damage trend and change in volume than pure heavy ion or He implantation.

The results and discussion in this work highlight the importance of continuing to develop a fundamental understanding of the synergistic effects of coupled extremes (e.g., two energetic beams) and demonstrate the significance of testing nuclear materials under reactor-similar conditions where two or more energetic beams or different extreme environments are simultaneously involved. This work will further promote experimental and modeling work from the materials and nuclear communities aiming to elucidate the synergistic effects of sequential and simultaneous irradiations.

Declaration of competing interest

The authors declare that they have no known competing financial interests or personal relationships that could have appeared to influence the work reported in this paper.

CRediT authorship contribution statement

O. El-Atwani: Conceptualization, Investigation, Funding acquisition, Writing - original draft. **W.S. Cunningham:** Formal analysis, Visualization, Writing - original draft. **J.R. Trelewicz:** Formal analysis, Writing - review & editing. **M. Li:** Investigation, Funding acquisition. **B.D. Wirth:** Methodology, Investigation, Writing - review & editing. **S.A. Maloy:** Conceptualization, Funding acquisition, Writing - review & editing.

Acknowledgements

This work was supported by the U.S. Department of Energy, Office of Nuclear Energy under DOE Idaho Operations Office Contract DE-AC07- 051D14517 as part of a Nuclear Science User Facilities experiment. Research presented in this article was also supported by the Laboratory Directed Research and Development program of Los Alamos National Laboratory under project number 20160674PRD3. WSC and JRT acknowledge support for this work from the National Science Foundation through grant 1810040 as well as the U.S. Department of Energy through grant DE-SC0017899. We gratefully acknowledge the support of the U.S. Department of Energy through the LANL/LDRD Program and the G. T. Seaborg Institute for this work. DP and EM acknowledge support by the U.S. Department of Energy, Office of Science, Office of Fusion Energy Sciences, and Office of Advanced Scientific Computing Research through the Scientific Discovery through Advanced Computing (SciDAC) project on Plasma—Surface Interactions under Award No. DE-SC0008875. BDW acknowledges partial support from the SciDAC project on Plasma Surface Interactions, as well as DOE Fusion Energy Sciences grant DE-SC-0006661.

Appendix A. Supplementary data

Supplementary data to this article can be found online at https://doi.org/10.1016/j.jnucmat.2020.152150.

References

[1] S.J. Zinkle, L.L. Snead, Designing radiation resistance in materials for fusion energy, Annu. Rev. Mater. Res. 44 (2014) 241—267.

[2] Y. Katoh, L. Snead, L. Garrison, X. Hu, T. Koyanagi, C. Parish, P. Edmondson, M. Fukuda, T. Hwang, T. Tanaka, Response of unalloyed tungsten to mixed spectrum neutrons, J. Nucl. Mater. 520 (2019) 193—207.

[3] S. Sharafat, A. Takahashi, Q. Hu, N.M. Ghoniem, A description of bubble growth and gas release of helium implanted tungsten, J. Nucl. Mater. 386—388 (2009) 900—903.

[4] M. Miyamoto, S. Mikami, H. Nagashima, N. Iijima, D. Nishijima, R.P. Doerner, N. Yoshida, H. Watanabe, Y. Ueda, A. Sagara, Systematic investigation of the formation behavior of helium bubbles in tungsten, J. Nucl. Mater. 463 (2015) 333—336.

[5] S. Kajita, N. Yoshida, R. Yoshihara, N. Ohno, M. Yamagiwa, TEM observation of the growth process of helium nanobubbles on tungsten: nanostructure formation mechanism, J. Nucl. Mater. 418 (1) (2011) 152—158.

[6] A. Al-Ajlony, J.K. Tripathi, A. Hassanein, Low energy helium ion irradiation induced nanostructure formation on tungsten surface, J. Nucl. Mater. 488 (2017) 1—8.

[7] M.J. Baldwin, R.P. Doerner, Formation of helium induced nanostructure 'fuzz' on various tungsten grades, J. Nucl. Mater. 404 (3) (2010) 165—173.

[8] S.J. Zinkle, G. Was, Materials challenges in nuclear energy, Acta Mater. 61 (3) (2013) 735—758.

[9] V. Philipps, Tungsten as material for plasma-facing components in fusion devices, J. Nucl. Mater. 415 (1) (2011) S2—S9.

[10] J. Knaster, A. Moeslang, T. Muroga, Materials research for fusion, Nat. Phys. 12 (5) (2016) 424—434.

[11] S. Kajita, W. Sakaguchi, N. Ohno, N. Yoshida, T. Saeki, Formation process of tungsten nanostructure by the exposure to helium plasma under fusion relevant plasma conditions, Nucl. Fusion 49 (9) (2009), 095005.

[12] O. El-Atwani, J. Hinks, G. Greaves, S. Gonderman, T. Qiu, M. Efe, J. Allain, In-situ TEM observation of the response of ultrafine-and nanocrystalline-grained tungsten to extreme irradiation environments, Sci. Rep. 4 (2014).

[13] O. El-Atwani, E. Esquivel, M. Efe, Y. Wang, S.A. Maloy, Detailed transmission electron microscopy study on the mechanism of dislocation loop rafting in tungsten, Acta Mater. 147 (2018) 277—283.

[14] V. Sikka, J. Moteff, "Rafting" in neutron irradiated tungsten, J. Nucl. Mater. 46 (2) (1973) 217—219.

[15] M. Efe, O. El-Atwani, Y. Guo, D.R. Klenosky, Microstructure refinement of tungsten by surface deformation for irradiation damage resistance, Scripta Mater. 70 (2014) 31—34.

[16] H. Kurishita, Y. Amano, S. Kobayashi, K. Nakai, H. Arakawa, Y. Hiraoka, T. Takida, K. Takebe, H. Matsui, Development of ultra-fine grained W—TiC and their mechanical properties for fusion applications, J. Nucl. Mater. 367 (2007) 1453—1457.

[17] Z. Xie, R. Liu, S. Miao, X. Yang, T. Zhang, X. Wang, Q. Fang, C. Liu, G. Luo, Y. Lian, Extraordinary high ductility/strength of the interface designed bulk W-ZrC alloy plate at relatively low temperature, Sci. Rep. 5 (2015), 16014.

[18] X. Tan, L. Luo, H. Chen, X. Zhu, X. Zan, G. Luo, J. Chen, P. Li, J. Cheng, D. Liu, Mechanical properties and microstructural change of W—Y 2 O 3 alloy under helium irradiation, Sci. Rep. 5 (2015), 12755.

[19] O. El-Atwani, E. Esquivel, E. Aydogan, E. Martinez, J. Baldwin, M. Li, B. Uberuaga, S. Maloy, Unprecedented irradiation resistance of nanocrystalline tungsten with equiaxed nanocrystalline grains to dislocation loop accumulation, Acta Mater. 165 (2019) 118—128.

[20] O.K. Donaldson, K. Hattar, T. Kaub, G.B. Thompson, J.R. Trelewicz, Solute stabilization of nanocrystalline tungsten against abnormal grain growth, J. Mater. Res. 33 (1) (2018) 68—80.

[21] O.A. Waseem, H.J. Ryu, Powder metallurgy processing of a W x TaTiVCr high-entropy alloy and its derivative alloys for fusion material applications, Sci. Rep. 7 (1) (2017) 1926.

[22] O. El-Atwani, N. Li, M. Li, A. Devaraj, J. Baldwin, M. Schneider, D. Sobieraj, J. Wróbel, D. Nguyen-Manh, S.A. Maloy, Outstanding radiation resistance of tungsten-based high-entropy alloys, Sci. Adv. 5 (3) (2019), eaav2002.

[23] C. Heintze, F. Bergner, M. Hernández-Mayoral, R. Kögler, G. Müller, A. Ulbricht, Irradiation hardening of Fe—9Cr-based alloys and ODS Eurofer: effect of helium implantation and iron-ion irradiation at 300 C including sequence effects, J. Nucl. Mater. 470 (2016) 258—267.

[24] D. Armstrong, P. Edmondson, S. Roberts, Effects of sequential tungsten and helium ion implantation on nano-indentation hardness of tungsten, Appl. Phys. Lett. 102 (25) (2013), 251901.

[25] O. El-Atwani, W. Cunningham, E. Esquivel, M. Li, J. Trelewicz, B. Uberuaga, S. Maloy, In-situ irradiation tolerance investigation of high strength ultrafine tungsten-titanium carbide alloy, Acta Mater. 164 (2019) 547—559.

[26] O. El-Atwani, A. Suslova, T. Novakowski, K. Hattar, M. Efe, S. Harilal, A. Hassanein, In-situ TEM/heavy ion irradiation on ultrafine-and nanocrystalline-grained tungsten: effect of 3MeV Si, Cu and W ions, Mater. Char. 99 (2015) 68—76.

[27] M. Li, M. Kirk, P. Baldo, D. Xu, B. Wirth, Study of defect evolution by TEM with in situ ion irradiation and coordinated modeling, Philos. Mag. A 92 (16) (2012) 2048—2078.

[28] X. Yi, M.L. Jenkins, M.A. Kirk, Z. Zhou, S.G. Roberts, In-situ TEM studies of 150 keV W+ ion irradiated W and W-alloys: damage production and microstructural evolution, Acta Mater. 112 (2016) 105—120.

[29] X. Yi, M.L. Jenkins, K. Hattar, P.D. Edmondson, S.G. Roberts, Characterisation of radiation damage in W and W-based alloys from 2MeV self-ion near-bulk implantations, Acta Mater. 92 (2015) 163—177.

[30] R. Harrison, J. Hinks, S. Donnelly, Influence of pre-implanted helium on dislocation loop type in tungsten under self-ion irradiation, Scripta Mater. 150 (2018) 61—65.

[31] R.W. Harrison, G. Greaves, J. Hinks, S. Donnelly, A study of the effect of helium concentration and displacement damage on the microstructure of helium ion irradiated tungsten, J. Nucl. Mater. 495 (2017) 492—503.

[32] X. Hu, T. Koyanagi, M. Fukuda, Y. Katoh, L.L. Snead, B.D. Wirth, Defect evolution in single crystalline tungsten following low temperature and low dose neutron irradiation, J. Nucl. Mater. 470 (2016) 278—289.

[33] J.F. Ziegler, M.D. Ziegler, J.P. Biersack, SRIM—The stopping and range of ions in matter, Nucl. Instrum. Methods Phys. Res. Sect. B Beam Interact. Mater. Atoms 268 (11) (2010) 1818—1823, 2010.

[34] A.E.-. e1, Standard Practice for Neutron Radiation Damage Simulation by Charged Particle Radiation, American society of testing and material Wes Conshohocken, PA, 2009.

[35] O. El-Atwani, E. Esquivel, M. Efe, E. Aydogan, Y. Wang, E. Martinez, S. Maloy, Loop and void damage during heavy ion irradiation on nanocrystalline and coarse grained tungsten: microstructure, effect of dpa rate, temperature, and

grain size, Acta Mater. 149 (2018) 206–219.

[36] M. Jenkins, Characterisation of radiation-damage microstructures by TEM, J. Nucl. Mater. 216 (1994) 124–156.

[37] F. Dausinger, H. Schultz, Long-range migration of self-interstitial atoms in tungsten, Phys. Rev. Lett. 35 (26) (1975) 1773.

[38] A. Debelle, M. Barthe, T. Sauvage, First temperature stage evolution of irradiation-induced defects in tungsten studied by positron annihilation spectroscopy, J. Nucl. Mater. 376 (2) (2008) 216–221.

[39] D. Reed, A review of recent theoretical developments in the understanding of the migration of helium in metals and its interaction with lattice defects, Radiat. EIT 31 (3) (1977) 129–147.

[40] O. El-Atwani, E. Esquivel, E. Aydogan, E. Martinez, J. Baldwin, M. Li, B.P. Uberuaga, S.A. Maloy, Unprecedented irradiation resistance of nanocrystalline tungsten with equiaxed nanocrystalline grains to dislocation loop accumulation, Acta Mater. 165 (2019) 118–128.

[41] W. Setyawan, G. Nandipati, K.J. Roche, H.L. Heinisch, B.D. Wirth, R.J. Kurtz, Displacement cascades and defects annealing in tungsten, Part I: defect database from molecular dynamics simulations, J. Nucl. Mater. 462 (2015) 329–337.

[42] K. Yabuuchi, M. Saito, R. Kasada, A. Kimura, Neutron irradiation hardening and microstructure changes in Fe–Mn binary alloys, J. Nucl. Mater. 414 (3) (2011) 498–502.

[43] B. Yao, D.J. Edwards, R.J. Kurtz, TEM characterization of dislocation loops in irradiated bcc Fe-based steels, J. Nucl. Mater. 434 (1–3) (2013) 402–410.

[44] R. Harrison, H. Amari, G. Greaves, J. Hinks, S. Donnelly, Effect of He-appm/DPA ratio on the damage microstructure of tungsten, MRS Adv. 1 (42) (2016) 2893–2899.

[45] B. Eyre, R. Bullough, On the formation of interstitial loops in bcc metals, Philos. Mag. A 12 (115) (1965) 31–39.

[46] C. English, M. Jenkins, Molecular ion irradiations of molybdenum, Philos. Mag. A 90 (7–8) (2010) 821–843.

[47] J. Marian, B.D. Wirth, J.M. Perlado, Mechanism of formation and growth of< 100> interstitial loops in ferritic materials, Phys. Rev. Lett. 88 (25) (2002), 255507.

[48] K. Arakawa, T. Amino, H. Mori, Direct observation of the coalescence process between nanoscale dislocation loops with different Burgers vectors, Acta Mater. 59 (1) (2011) 141–145.

[49] X. Gai, T. Lazauskas, R. Smith, S.D. Kenny, Helium bubbles in bcc Fe and their interactions with irradiation, J. Nucl. Mater. 462 (2015) 382–390.

[50] C.S. Deo, M.A. Okuniewski, S.G. Srivilliputhur, S.A. Maloy, M.I. Baskes, M.R. James, J.F. Stubbins, The effects of helium on irradiation damage in single crystal iron, J. Nucl. Mater. 367 (2007) 451–456.

[51] F. Sefta, K.D. Hammond, N. Juslin, B.D. Wirth, Tungsten surface evolution by helium bubble nucleation, growth and rupture, Nucl. Fusion 53 (7) (2013), 073015.

[52] M.A. El Keriem, D. Van Der Werf, F. Pleiter, Helium-vacancy interaction in tungsten, Phys. Rev. B 47 (22) (1993), 14771.

[53] J. Vetrano, I. Robertson, M. Kirk, Experimental evidence favoring local melting within heavy-ion generated displacement cascades in copper, Scripta Metall. Mater. 24 (1) (1990) 157–162.

[54] M. Jenkins, M. Kirk, W. Phythian, Experimental studies of cascade phenomena in metals, J. Nucl. Mater. 205 (1993) 16–30.

[55] N.A. Capps, Molecular Dynamics Simulations of Cascade Evolution Near Pre-existing Defects, 2013.

[56] D. Mason, X. Yi, M. Kirk, S. Dudarev, Elastic trapping of dislocation loops in cascades in ion-irradiated tungsten foils, J. Phys. Condens. Matter 26 (37) (2014), 375701.

[57] P.M. Anderson, J.P. Hirth, J. Lothe, Theory of Dislocations, Cambridge University Press, 2017.

[58] A.A. Kohnert, L. Capolungo, Sink strength and dislocation bias of three-dimensional microstructures, Phys. Rev. Mater. 3 (5) (2019), 053608.

[59] O. El-Atwani, E. Martinez, E. Esquivel, M. Efe, C. Taylor, Y. Wang, B. Uberuaga, S. Maloy, Does sink efficiency unequivocally characterize how grain boundaries impact radiation damage? Phys. Rev. Mater. 2 (11) (2018), 113604.

[60] N. Juslin, V. Jansson, K. Nordlund, Simulation of cascades in tungsten–helium, Philos. Mag. A 90 (26) (2010) 3581–3589.

[61] C. Becquart, B. Wirth, Kinetic Monte Carlo Simulations of Irradiation Effects, 2012.

[62] Z. Zhang, K. Yabuuchi, A. Kimura, Defect distribution in ion-irradiated pure tungsten at different temperatures, J. Nucl. Mater. 480 (2016) 207–215.

[63] M. Wen, N.M. Ghoniem*, B.N. Singh, Dislocation decoration and raft formation in irradiated materials, Philos. Mag. A 85 (22) (2005) 2561–2580.

[64] J.S. Weaver, C. Sun, Y. Wang, S.R. Kalidindi, R.P. Doerner, N.A. Mara, S. Pathak, Quantifying the mechanical effects of He, W and He+ W ion irradiation on tungsten with spherical nanoindentation, J. Mater. Sci. 53 (7) (2018) 5296–5316.